RSC Advances

PAPER

View Article Online
View Journal | View Issue

Cite this: *RSC Adv.*, 2025, **15**, 3098

A free-radical initiator-based carrier-free smart nanobomb for targeted synergistic therapy of hypoxic breast cancer†

Liefeng Hu, *[ab] Ganlin Dong,[b] Xiaohong Li,[b] Shuting Li*[c] and Yonggang Lv*[b]

Thermodynamic therapy (TDT) is a promising alternative to photodynamic therapy (PDT) by absorbing heat through thermosensitive agents (TSAs) to generate oxygen-irrelevant highly toxic free radicals. Therefore, TDT can be a perfect partner for photothermal therapy (PTT) to achieve efficient synergistic treatment of anoxic tumors using a single laser, greatly simplifying the treatment process and overcoming hypoxia limitations. However, the issues of how to improve the stability and delivery efficiency of TSAs still need to be addressed urgently. Herein, polyethylene glycol–folic acid (PEG–FA)-modified and indocyanine green (ICG)-encapsulated nanoscale Zn^{2+} and 2′-azobis[2-(2-imidazolin-2-yl)propane] dihydrochloride (AIPH) coordinated nanomaterials (IANM-PEG-FA) were developed as a nanobomb for targeted photothermal/thermodynamic/ion-interference cancer therapy. Co-triggered by a single 808 nm laser and mildly acidic tumor microenvironment, the photothermal agent of ICG would induce rapid decomposition of AIPH to generate alkyl radicals and release ICG and Zn^{2+}, resulting in effectively cascaded oxygen-independent photothermal/thermodynamic therapy and co-enhanced synergistic intracellular overload of Zn^{2+} interference. Additionally, PEG–FA enabled favorable stability and active targeting ability to achieve low side effects and efficient tumor enrichment for good photothermal/near-infrared fluorescence imaging-guided precise tumor therapy. Significantly, the IANM-PEG-FA nanosystem exhibited remarkable anticancer effects even at low doses in hypoxic breast cancer, achieving 80% tumor elimination. Our study might provide a highly effective strategy for developing a multifunctional carrier-free nanosystem with high performance in hypoxic cancer to meet the requirements in the clinic.

Received 4th November 2024
Accepted 15th January 2025

DOI: 10.1039/d4ra07841a

rsc.li/rsc-advances

Introduction

Phototherapy, including photothermal therapy (PTT) and photodynamic therapy (PDT), has received promising outcomes in preclinical and clinical anti-tumor applications due to its high therapeutic efficiency, spatiotemporal selectivity, and minimal invasion.[1–3] Phototherapy relies heavily on photosensitive agents, mainly referring to photothermal agents (PTAs) and photosensitizers (PSs).[4–6] PTAs exposed to a laser with a specific wavelength can increase the local temperature to destroy carcinomatous cells and tissues; alternatively, PSs can harvest light energy and transfer it to the surrounding oxygen (O_2), especially singlet oxygen species ($^1O_2$), which can cause apoptosis and necrosis of cancer cells.[7,8] PDT is oxygen-dependent, while PTT is not related to oxygen and shows great potential in the treatment of hypoxic tumors.[9] However, tumor cells exposed to hyperthermia will express heat shock proteins (HSPs) to develop thermotolerance that renders PTT ineffective.[10,11] Recently, the combined strategy of PTT and PDT was widely used to improve therapeutic outcomes through their independent anti-tumor mechanisms.[12–14] Most of the studies achieved the synergistic anti-tumor effects of PTT and PDT through the integration of discrete PS and PTA with different irradiation wavelengths on a single nanoplatform, which requires two light sources to excite the PS and PTA, complicating the preparation processes and practical operation.[15,16] In addition, the anti-tumor effect obtained by this strategy was usually "1 + 1 < 2" due to the inevitable limitations of each treatment modality, which did not significantly increase the efficiency of tumor therapy.[17,18] Therefore, it is desirable to develop a combined strategy that can conveniently achieve the anti-tumor efficiency of "1 + 1 > 2".

Thermodynamic therapy (TDT) is a promising alternative to PDT by absorbing heat through thermosensitive agents to generate oxygen-irrelevant highly toxic free radicals.[19–21] TDT

[a]School of Materials Science and Engineering, Hubei Key Laboratory for New Textile Materials and Applications, Wuhan Textile University, Wuhan, 430200, P. R. China. E-mail: lfhu@wtu.edu.cn

[b]State Key Laboratory for New Textile Materials & Advanced Processing Technology, Wuhan Textile University, Wuhan, 430200, P. R. China. E-mail: yglv@wtu.edu.cn

[c]School of Physical Education, Equine Science Research and Doping Control Center, Wuhan Business University, Wuhan 430056, China. E-mail: list1224@163.com

† Electronic supplementary information (ESI) available. See DOI: https://doi.org/10.1039/d4ra07841a

can be a perfect partner for PTT to achieve efficient synergistic treatment of anoxic tumors using a single laser, where TDT can be sparked *in situ* by PTT to eradicate cancer cells.[22,23] Currently, 2,2′-azobis[2-(2-imidazolin-2-yl)propane]-dihydrochloride (AIPH) is of great interest as a radical initiator because of its rapid decomposition under thermal triggering to produce alkyl radicals, which induces cell death through DNA damage, lipid and protein peroxidation.[24,25] However, there are still two aspects that need urgent improvement: (1) AIPH is suspected to break down *in vivo* due to its instability and toxic side effects, and (2) low loading capacity and bioavailability of AIPH.[26–29] It is thereby of great importance to develop a biocompatible nanosystem with high loading efficiency and controllable release of AIPH for highly efficient targeted therapy of hypoxic cancers.

Carrier-free nanosystems (CFNs) are a kind of drug delivery system (DDS) self-constructed from therapeutic agents without inert materials, which have attracted much attention in cancer therapy due to the integrated superiorities of the simplified preparation process, low systemic toxicity, high payload ability, intelligent response features, and multifunctional platform potential.[30–33] As with other conventional delivery nanosystems, insufficient enrichment of CFNs at the tumor site and undesirable side effects due to the lack of active targeting and controllable release remain the major challenges for preclinical translation.[34–36] To improve the performances of precise tumor treatments and minimize the toxicity of non-targeted delivery to normal cells, many efforts have been devoted to developing nanosystems with tumor-targeting and/or stimulus responsiveness of internal and external sources.[37–39] On the other hand, CFNs offer an "all in one" platform for tackling complex tumor environments, demonstrating great potential for clinical translation.[40,41]

Herein, we proposed a free-radical initiator-based cancer-targeted nanoscale metal–organic complex (MOC) as the CFN for highly efficient multimodal photothermal/thermodynamic/ion-interference therapy in hypoxic tumors (Scheme 1). The CFN was based on AIPH as a therapeutic agent prepared by a one-pot method with efficient loading of ICG molecules during the coordination process between Zn^{2+} and AIPH, and further modified using polyethylene glycol–folic acid (PEG–FA) (namely

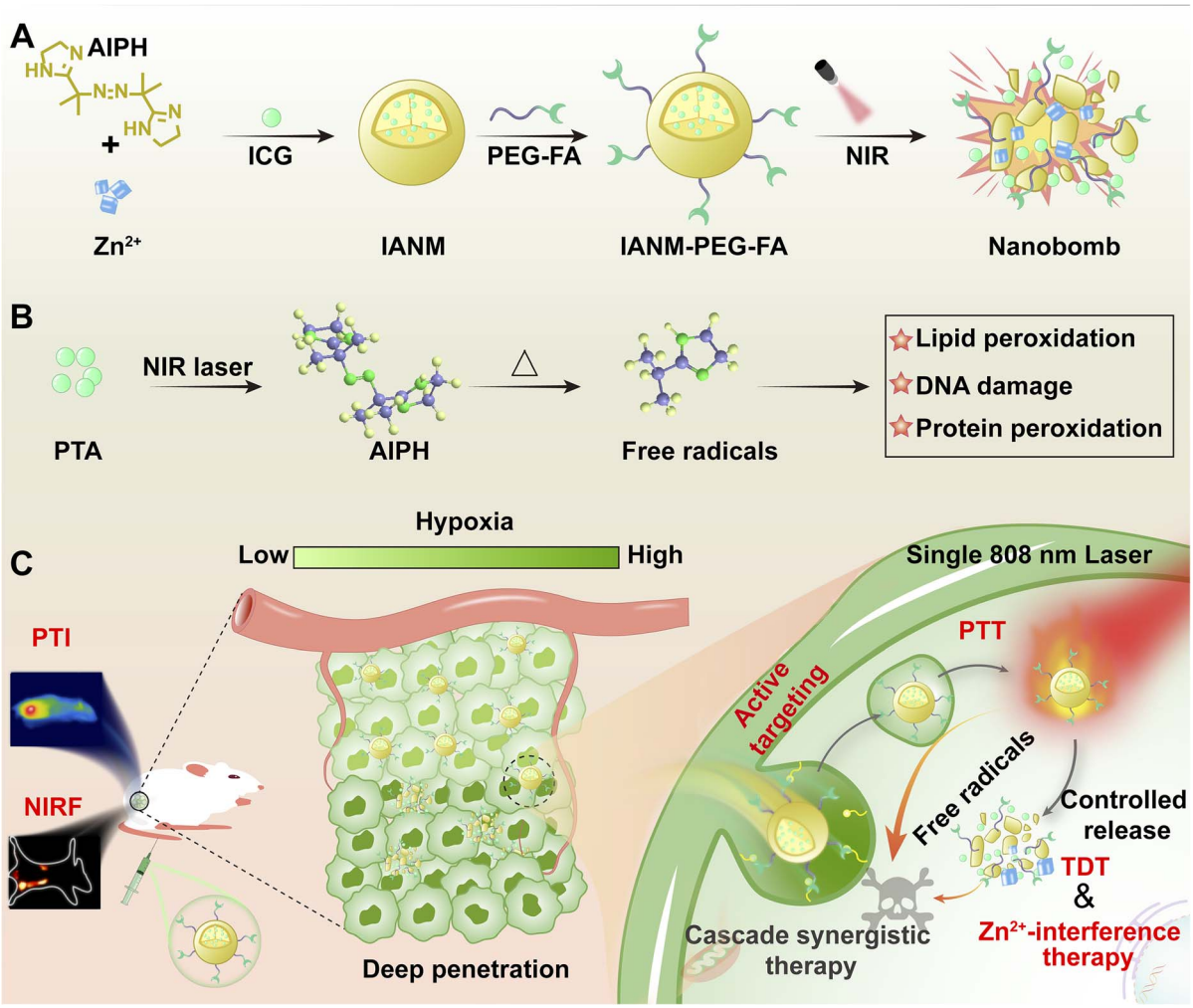

Scheme 1 Schematic illustration of the IANM-PEG-FA NPs for multimodal anti-tumor. (A) Preparation process of IANM-PEG-FA and the diagram of NIR-mediated nanobomb effects. (B) The therapeutic mechanisms of AIPH as the thermodynamic agent. (C) Schematic diagram of IANM-PEG-FA targeting of tumor cells and trimodal oxygen-irrelevant photothermal/thermodynamic/ion interference hypoxic tumor therapy.

IANM-PEG-FA). IANM-PEG-FA could circulate stably in the blood and identify tumor cells for efficiently targeted enrichment due to the modification of PEG–FA. Spatiotemporal selective irradiation of tumor sites with near-infrared light not only enabled the ICG to perform PTT but also stimulated the production of alkyl radicals by the AIPH to achieve highly effective sequential TDT. Moreover, the tumor site-specific mildly acidic environment induced the nanosystem to responsively disintegrate and release Zn^{2+}, ICG, and alkyl radicals, thus acting like a nanobomb for large-scale ion-interference therapy and TDT. Significantly, each therapeutic mode in the sequential synergistic enhancement strategy of this nanosystem was irrelevant to oxygen, effectively conquering the tumor hypoxic environment and demonstrating multimodal imaging-guided good anti-tumor effects with a cure rate of 80% at low doses. The novel CFN based on radical initiators greatly simplified the preparation process and improved the tumor treatment efficiency, showing promise for preclinical and clinical applications.

Experimental

Preparation of IANM-PEG-FA

IANM-PEG-FA was prepared by a facile self-assembly coordination strategy Typically, 50 μL TEA was added into 5 mL of DMF solution containing 3 mg of AIPH at room temperature, followed by the addition of ICG (2 mg). Then, the DMF solution of $Zn(NO_3)_2 \cdot 6H_2O$ (24 mg, 2 mL) was quickly mixed with the above solution and gently stirred at ambient temperature for 10 min. The mixed solution became an emulsion and was collected by centrifugation (10 000 rpm, 15 min), followed by repeated DMF/water washing before dispersion in water to obtain the resulting IANM. PEG–FA was next modified into the IANM nanosystem. 1 mL PEG–FA aqueous solution (1 mg) and 2 mL IANM aqueous solution (1 mg mL^{-1}) were mixed and stirred at room temperature for 24 h, followed by three washes by centrifugation with water. Then the obtained IANM-PEG-FA nanoparticles were redispersed into water for further use.

Cascade photothermal degradation assessment of IANM-PEG-FA

As AIPH is degraded by heat and produces alkyl radicals. The degradation, thermodynamic and cargo release features of IANM-PEG-FA were next explored. The morphology of IANM-PEG-FA before and after near-infrared laser irradiation was observed by transmission electron microscopy (TEM). The free radical generation detection experiments were performed by irradiating IANM-PEG-FA containing different concentrations of ICG by 1 W cm^{-2} 808 nm laser using DMPO as a detection probe. Moreover, the free radical generation of IANM-PEG-FA was also evaluated in different temperature environments. Besides, the photothermal cascade alkyl radicals production of IANM-PEG-FA was fully characterized by electron spin resonance (ESR). Furthermore, the cumulative release of ICG from IANM-PEG-FA under different temperature and pH conditions was evaluated to verify the smart responsiveness of this nanosystem.

In vitro cellular cytotoxicity

The responsive degradation properties of IANM-PEG-FA resulted in the release of Zn^{2+}, which could interfere with the normal growth of tumor cells and lead to cell death once the concentration was too high, this phenomenon was ion-interference therapy.[42] Briefly, 4T1 cell lines (mouse breast cancer cells) were cultured under normoxic and hypoxic environments at a density of 10^4 cells per well in 96-well plates for 24 h. A fresh culture medium containing serial concentrations of IANM-PEG-FA (0–400 μg mL^{-1}) was added to each well to incubate with cells for another 24 h, and then the fresh culture medium containing 5 mg per mL MTT was added to incubate for another 4 h to generate formazan crystals. The purple formazan crystals in each well were dissolved by 150 μL DMSO and the absorbance was detected on a microplate reader at a wavelength of 490 nm.

Cascade PTT and TDT *in vitro*

4T1 cell lines were seeded in normoxia and hypoxia at a density of 10^4 cells per well in 96-well plates for 24 h. Then, a fresh medium containing various concentrations of IANM-PEG-FA (0–100 μg mL^{-1}) was added to incubate for another 24 h. The cells in cascade PTT and TDT were exposed to an 808 nm laser at the power density of 1 W cm^{-2} for 3 min. Ascorbic acid (Vitamin C, Vc) as an antioxidant could efficiently scavenge the ROS. While the single PTT groups were pre-treated with Vc (Vc, 2×10^{-3} M) and then irradiated by 1 W cm^{-2} 808 nm laser for 3 min. The cells in the Control groups without light exposure remained in the dark. After being further incubated for another 24 hours, the viabilities of cells were measured by the standard MTT assays mentioned above. The therapeutic effects against 4T1 cells were also measured by CLSM and flow cytometry using live/dead cell double-staining fluorescent probes and apoptosis kit, respectively.

Pharmacokinetic and biodistribution analysis

Female BALB/c mice (16–18 g) were purchased from the Experimental Animal Center of Huazhong Agricultural University. Firstly, healthy female BALB/c mice were intravenously injected with 100 μL IANM-PEG-FA (dose: 5 mg kg^{-1}). Blood (10 μL) was collected from the tail veins at different time points (I_t). The initial concentration (I_0) of IANM-PEG-FA was obtained by measuring the fluorescence intensity of the first blood sample (10 μL blood, 10 μL heparin sodium solution and 980 μL purified water). The intensity of blood fluorescence imaging was also further observed by the NIR imager. The *in vivo* circulating half-life of IANM-PEG-FA was calculated by a ratio of fluorescent intensity (I_t/I_0). For biodistribution analysis, 4T1 tumor-bearing female BALB/c mice were injected with 100 μL IANM-PEG-FA (dose: 5 mg kg^{-1}) *via* the tail vein. The mice were observed by the NIR imager to monitor the fluorescence distribution.

Hypoxic breast cancer therapy *in vivo*

The mice were randomly divided into four treatment groups with IANM-PEG-FA plus laser irradiation (PTT + TDT), Saline plus laser irradiation (Saline + L), only IANM-PEG-FA injection

(IANM-PEG-FA) ($n = 5$), and one group of IANM-PEG-FA plus Vc pre-treatment and laser irradiation for single PTT. 4T1 tumor-bearing mice were injected with 100 μL of 0.5 mg per mL IANM-PEG-FA through the tail vein. After IANM-PEG-FA and Saline injection for 12 h, the tumor sites were irradiated with the 808 nm laser at power densities of 1 W cm^{-2} for 5 min. The tumor sizes and body weights were measured by a caliper each day for 15 days. The tumor volumes were calculated according to the following equation: (tumor width)^2 × (tumor length)/2, and mice were executed once the tumor volume exceeded 1000 mm^3.

Live subject statement

All animal procedures were performed in accordance with the Guidelines for Care and Use of Laboratory Animals of the Institutional Animal Care and Use Committee of Huazhong Agricultural University and approved by the Animal Ethics Committee of the Chinese Regulations for the Administration of Affairs Concerning Experimental Animals (Animal ethics number: HZAUMO-2023-0311).

Results and discussion

Preparation and characterization of IANM-PEG-FA

The novel CFN with high radical initiator assembly and post-modification of targeted moiety (IANM-PEG-FA) was schematically illustrated in Scheme 1. Firstly, IANM efficiently loaded with ICG was prepared by a one-pot method *via* the coordination between Zn^{2+} and the ligands of AIPH. Then, the modification of FA-conjugated PEG chains enabled the obtained IANM-PEG-FA not only to possess the active tumor targeting ability but also significantly improved the biocompatibility and physiological stability. As shown in Fig. 1A–D, the prepared ANM and IANM-PEG-FA nanoparticles (NPs) were measured by transmission electron microscopy (TEM) and dynamic light scattering (DLS) measurements. Homogeneously dispersed ANM and IANM-PEG-FA were successfully prepared; the inset showed that ANM appeared as a white emulsion, while IANM-PEG-FA showed the green color of ICG. The size increased obviously from 68.8 ± 3.2 nm to 159.4 ± 2.7 nm with the encapsulation of ICG and the modification of PEG–FA. Besides, the zeta potential of IANM-PEG-FA NPs changed from 9.4 ± 1.3 mV for ANM and 1.4 ± 0.5 mV for IANM NPs to −2.4 ± 0.1 mV. Negatively charged IANM-PEG-FA NPs were favorable for tumor accumulation as they form a stable colloidal system and increase enrichment in tumor tissue. As shown in Fig. 1E, the ultraviolet-visible (UV-vis) absorbance spectrum of IANM-PEG-FA exhibited the characteristic peaks of both ICG and ANM, indicating the successful encapsulation of ICG. The loading content (LC) of ICG was further evaluated by different feed ratios. As displayed in Fig. S1,† the LC gradually increased with increasing ICG in the range of proportions tested, reaching a maximum of 47.2 ± 2.04% at 1 : 0.67. In addition, Fourier Transform Infrared Spectroscopy (FTIR) was employed to identify the structure of IANM-PEG-FA (Fig. S2†). The size changes of IANM-PEG-FA in water at 25 °C and Dulbecco's Modified Eagle Medium (DMEM) containing 10% fetal bovine serum (FBS) at 37 °C were measured to evaluate its stability for storage and biomedical applications. The particle size fluctuation was negligible after one week of incubation in the medium, indicating good stability of IANM-PEG-FA (Fig. 1F).

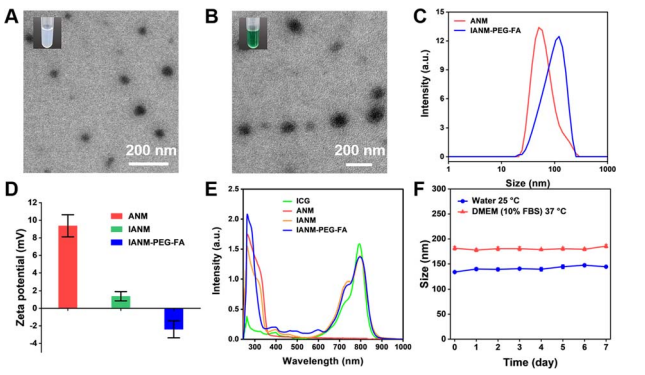

Fig. 1 Characterization of IANM-PEG-FA. The representative TEM images of (A) ANM and (B) IANM-PEG-FA NPs, respectively. (C) Hydrodynamic diameters of ANM and IANM-PEG-FA NPs in water. (D) Changes in zeta potential of ANM, IANM, and IANM-PEG-FA NPs. (E) The UV-vis absorption spectrum of ICG, ANM, IANM and IANM-PEG-FA. (F) The size stability curves of IANM-PEG-FA in different media for 7 days. Data are presented as mean values ± S.D. ($n = 3$).

Cascade photothermal and thermodynamic properties and cargo release profile

Next, the photothermal performances and cascade thermodynamic properties of IANM-PEG-FA were measured under a single near-infrared (NIR) laser excitation due to the strong NIR absorption of ICG. As shown in Fig. 2A, the temperature changes of different concentrations of IANM-PEG-FA dispersed in deionized water were recorded by a thermal imaging camera after irradiation with a 1 W cm^{-2} 808 nm laser for 3 min. A negligible temperature increase was seen in the group of pure water, suggesting that water could not harvest the 808 nm laser energy and convert it into heat. The temperature increase profile of the IANM-PEG-FA NPs exhibited a concentration-dependent variation manner, and the highest temperature of IANM-PEG-FA containing 30 μg per mL ICG reached 65.2 °C. The physical and thermographic images of the sample solutions at different concentrations after 3 minutes of laser irradiation are shown simultaneously in Fig. 2B. Moreover, the photothermal performances of IANM-PEG-FA NPs displayed the laser-power-density-dependent (Fig. S3†). It is well known that ICG as a PTA suffers from the drawbacks of photobleaching and photoinstability. Therefore, the photothermal stability of IANM-PEG-FA was further evaluated and compared with ICG. As presented in Fig. 2C, the stability of IANM-PEG-FA was significantly improved under 1 W cm^{-2} 808 nm laser irradiation with three heating and cooling cycles. The temperature of the ICG molecule rapidly decreased from 63.1 °C to 43.4 °C after three cycles with an obvious photobleaching phenomenon. Subsequently, the corresponding absorption spectra of ICG and IANM-PEG-FA were recorded during the cycling process, and the results showed that IANM-PEG-FA could effectively enhance the

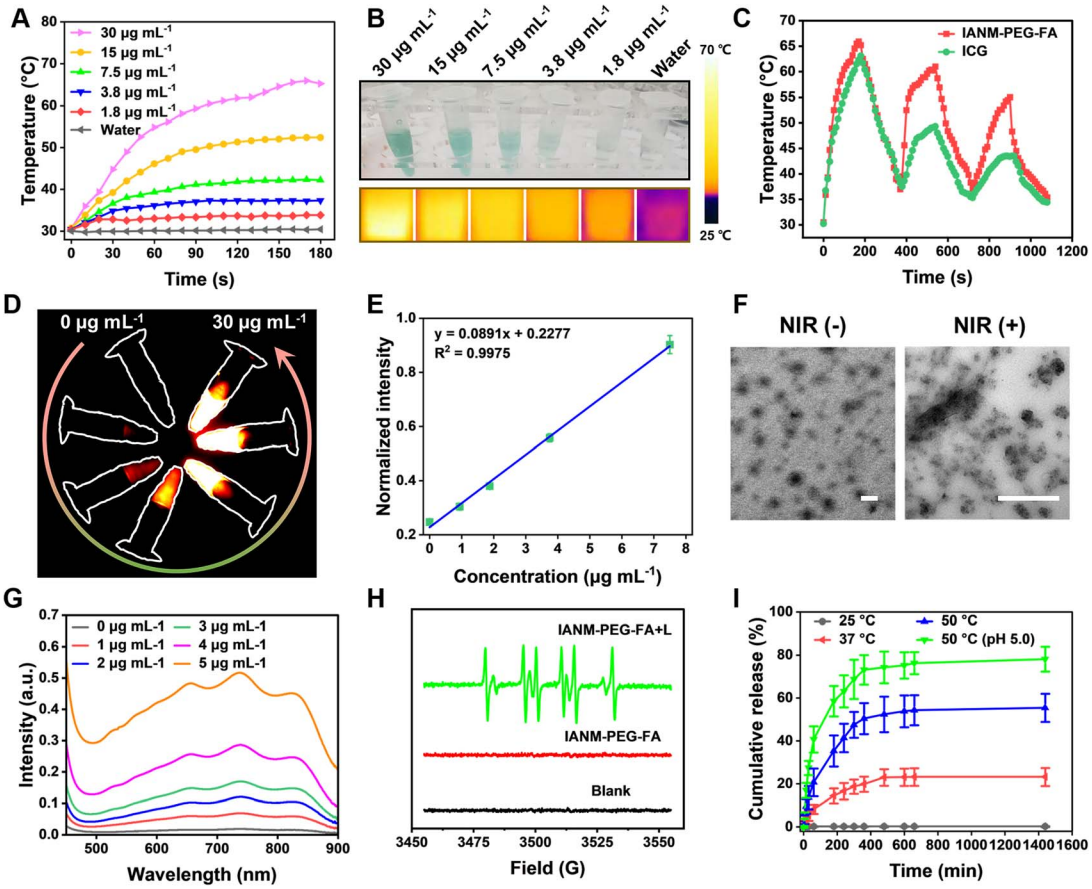

Fig. 2 Characterization of anti-tumor properties of IANM-PEG-FA. (A) Temperature elevation of IANM-PEG-FA in water in dependence of concentration (808 nm, 1 W cm^{-2}). (B) Optical graphs and thermal images of IANM-PEG-FA in water at different concentrations. (C) Photothermal stability of IANM-PEG-FA containing 30 μg per mL ICG for three irradiation cooling cycles (1.0 W cm^{-2}), 30 μg per mL ICG molecule aqueous solution as reference. (D) NIR fluorescence imaging of IANM-PEG-FA containing different concentrations of ICG (0–30 μg mL^{-1}) in aqueous solution. (E) Standard curve of fluorescence intensity of IANM-PEG-FA containing different ICG concentrations (0–7.5 μg mL^{-1}). (F) TEM images of morphological changes of IANM-PEG-FA after 1 W cm^{-2} 808 nm laser irradiation. The scale bar was 250 nm. (G) The spectra of $ABTS^{+\bullet}$ in the presence of IANM-PEG-FA containing 0–5 μg mL^{-1} ICG and 1 W cm^{-2} 808 nm laser irradiation. (H) ESR spectra of the blank group, IANM-PEG-FA, and IANM-PEG-FA plus 5 min laser irradiation group in the presence of DMPO. (I) The cumulative release of ICG from IANM-PEG-FA in aqueous media with different environments. Data are presented as mean values ± S.D. ($n = 3$).

stability of ICG for further applications. Besides, ICG could be used as a contrast agent for NIR fluorescence imaging. As shown in Fig. 2D, different concentrations of IANM-PEG-FA were detected by the 880 nm long-wavelength (LP) filter of the NIR imager, and the fluorescence intensity gradually increased with the increase of ICG content (0–30 μg mL^{-1}) in IANM-PEG. A positive linear correlation between NIR fluorescence intensity and IANM-PEG-FA concentration was obtained by semi-quantitative analysis (Fig. 2E), which could be used for quantitative fluorescence imaging. These results confirmed the good NIR fluorescence imaging and photothermal properties of IANM-PEG-FA, which could effectively activate thermodynamic radical initiators for cascade TDT. Then, the morphological changes of IANM-PEG-FA before and after 808 nm laser irradiation were observed by TEM. As shown in Fig. 2F, IANM-PEG-FA NPs disintegrated after laser irradiation and generated many small fragments. AIPH in IANM-PEG-FA NPs was stimulated by 808 nm laser irradiation-mediated photothermal effect to produce alkyl radicals and detected using 2,2′-azino-bis(3-ethylbenzothiazoline-6-sulfonic acid) (ABTS) as the probe, which would be sensitized to a green $ABTS^{+\bullet}$ solution with a characteristic absorbance range from 500 to 900 nm. As illustrated in Fig. 2G, as the ICG concentration of IANM-PEG-FA increased, the characteristic absorption peaks of $ABTS^{+\bullet}$ became stronger, suggesting that IANM-PEG-FA could achieve effective combined photothermal and thermodynamic effects by a single laser irradiation. Further studies were carried out on the generation of $ABTS^{+\bullet}$ from IANM-PEG-FA after incubation for 2, 4, 8, and 12 min in different temperature environments (25, 37, and 50 °C). As shown in Fig. S4,† the absorbance of $ABTS^{+\bullet}$ showed incubation temperature and time dependence, and was significantly higher at 50 °C than at 25 °C and 37 °C, revealing the efficient decomposition and yielding of AIPH radicals under heating conditions. The generation of alkyl radicals under 808 nm laser irradiation was further assessed by electron spin resonance (ESR) measurements using 5,5-dimethyl-1-pyrroline *N*-oxide (DMPO) as a probe. As depicted in Fig. 2H, the IANM-PEG-FA plus laser irradiation (IANM-PEG-FA

+ L) group exhibited obvious DMPO/alkoxyl additive signals, while no signal was found in the other groups. These results indicated that IANM-PEG-FA could achieve highly efficient combined photothermal and thermodynamic effects with a single laser irradiation. Thermally-induced AIPH degradation also achieved a controlled release effect. As shown in Fig. 2I, the cumulative release of ICG was relevant to the temperature, and the final cumulative release rate was 55.4 ± 6.57% at 50 °C, but only 23.13 ± 4.23% and 0.13 ± 0.21% at 37 °C and 25 °C, respectively. Besides, a mildly acidic environment (pH 5.0) could further increase the release of ICG, which reached a cumulative release rate of 78.1 ± 5.79%. IANM-PEG-FA NPs exhibited dual heat- and pH-responsive controlled release profiles, which could be used as a delivery platform to achieve precise and efficient anti-tumor effects.

Cellular uptake and delivery of IANM-PEG-FA *in vitro*

4T1 cell line, a typical breast cancer cell line, is widely used in cancer therapy research due to its high degree of hypoxia. Therefore, the internalization of IANM-PEG-FA was studied by confocal laser scanning microscope (CLSM) in 4T1 cell lines. As shown in Fig. 3A, the red fluorescence signal attributed to ICG was gradually enhanced with the prolongation of the co-incubation time (1–4 h) between IANM-PEG-FA nanomaterials and cells, indicating the efficient internalization of IANM-PEG-FA. Interestingly, more red fluorescence signals were found in the nucleus at 4 hours, indicating that ICG was delivered into the nucleus, which might be caused by the degradation of IANM-PEG-FA stimulated by the acidic environment in the cell and the release of ICG. This phenomenon has been widespread in efficient drug delivery strategies to conquer multidrug resistance. Meanwhile, the cellular uptake at different incubation times was quantified by flow cytometry (Fig. 3B). Compared with the Control group, the cellular uptake of IANM-PEG-FA reached 53.6%, 57.1%, and 78.6%, respectively, with the extension of culture time. The 4T1 cell-targeted uptake effect of IANM-PEG-FA was further explored. As displayed in Fig. 3C, after co-incubating IANM-PEG-FA NPs with 4T1 cells for 3 hours, the red fluorescent signal of ICG was mainly distributed in the cytoplasm, suggesting that IANM-PEG-FA could be efficiently ingested by 4T1 cells. The fluorescence intensity of ICG was significantly decreased after pre-treatment of 4T1 cells with FA to block the targeting receptor, suggesting that IANM-PEG-FA NPs enhance uptake by recognizing the FA receptor. Subsequently, the cellular uptake of different groups (Control, IANM-PEG-FA, and FA-blocked groups were indicated as G1, G2, and G3, respectively) was quantified using flow cytometry. As displayed in Fig. 3D, the cell uptake rate of G2 reached 95.0%, while the uptake rate of G3 significantly decreased to 32.7%, further confirming that the PEG–FA modification endowed IANM-PEG-FA NPs with the 4T1 cell-targeting capacity to enhance internalization. The fluorescence effect plot of cellular uptake observed by CLSM was assessed by a semi-quantitative assessment of its uptake variability, demonstrating the superiority of IANM-PEG-FA-mediated targeting of 4T1 cells (Fig. S5†). Lysosomal escape of IANM-PEG-FA NPs visualized by CLSM

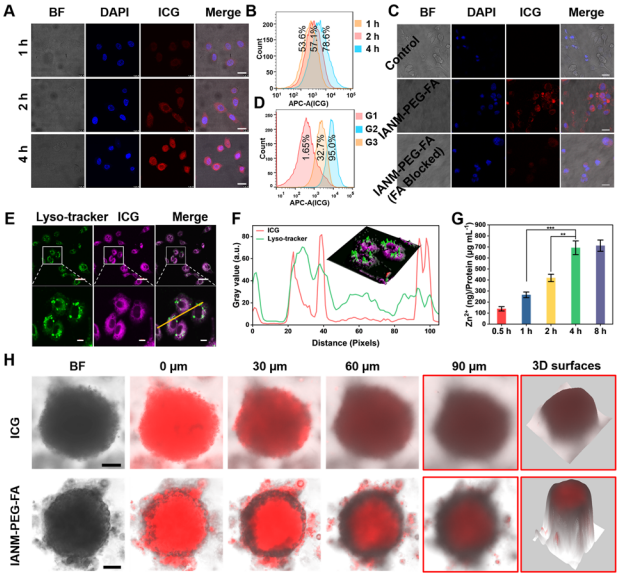

Fig. 3 Drug delivery effects of IANM-PEG-FA *in vitro*. (A) The representative CLSM images of 4T1 cells absorbed IANM-PEG-FA at various time points. The scale bar was 25 μm. (B) The quantitation of cellular uptake at different time points was measured by flow cytometry. (C) The CLSM images of FA-mediated targeted cellular uptake of IANM-PEG-FA at 3 hours. The scale bar was 25 μm. (D) The quantification of targeted cellular uptake of IANM-PEG-FA. G1, G2, and G3 denoted Control, IANM-PEG-FA, and IANM-PEG-FA (FA blocked) groups, respectively. (E) CLSM images of the escape effect of IANM-PEG in cellular lysosomes, the green color represented lysosomal tracker (Lyso-tracker) and the pink was the fluorescence of ICG. The scale bar was 50 μm and 10 μm, respectively. Similar images were obtained through more than three times experiments. (F) The localization effect was analyzed semi-quantitatively using ImageJ. The fluorescence intensity of the yellow line marker and cell surface fluorescence (inset) were assessed separately. (G) Intracellular Zn^{2+} concentration at different time intervals was assessed by ICP-MS. (H) The CLSM images of the effect of MCs penetration and 3D surface map at 90 μm depth. The scale bar was 50 μm. Data are presented as mean values ± S.D. ($n = 3$), and P values are calculated by a two-tailed Student's t-test. $^{**}P < 0.01$; $^{***}P < 0.001$.

using a lysosomal green fluorescent probe (Lyso-tracker). As performed in Fig. 3E, after incubating IANM-PEG-FA with 4T1 cells for 3 hours, the lysosomes stained with green fluorescence almost separated from the pink channel fluorescence of ICG, revealing that IANM-PEG-FA could avoid lysosomal catabolism and thus failure. The spatial separation effect could be visualized directly from the fluorescence localization images (Fig. 3F). Meanwhile, the effective cell internalization of IANM-PEG-FA was further confirmed by the detection of intracellular Zn^{2+} content, which reached the highest level at 4 hours. To demonstrate the superiorities of this nano-delivery system, the penetration effect was studied using multicellular spheres (MCs), which were widely used to simulate the solid tumor environment. As depicted in Fig. 3G, IANM-PEG-FA had shown significantly deeper penetration than ICG molecules at 30 μm and exhibited high fluorescence intensity even at the 90 μm layer, which was attributed to the pH-responsive delivery mechanism of IANM-PEG-FA. The full-scan image of the multicellular spheres also amply demonstrated that IANM-PEG-

FA exhibited deeper penetration ability (Fig. S6†). These results strongly demonstrated that IANM-PEG-FA could be efficiently absorbed by 4T1 cells and delivered into deeper tumor tissues with a higher degree of hypoxia, thus maximizing oxygen-independent antitumor effects.

Antitumor effects of IANM-PEG-FA *in vitro*

Therefore, the *in vitro* anti-tumor potential of IANM in a hypoxic environment was further investigated using 4T1 cells. First, the intracellular alkyl radicals generated by IANM-PEG-FA-NPs under 808 nm laser irradiation were detected using 2′,7′-dichlorodihydrofluorescein diacetate (DCFH-DA) as the fluorescent probe of reactive oxygen species (ROS). As shown in Fig. 4A, the 4T1 cell groups untreated with IANM-PEG-FA NPs did not show obvious green fluorescence in both normoxic and hypoxic environments with and without laser irradiation, indicating that 4T1 cells irradiated by 808 nm laser did not produce additional ROS. After the cell groups treated with IANM-PEG-FA upon 808 nm laser irradiation for 5 min, bright green fluorescence was seen in both hypoxia and normoxia, whereas only negligible fluorescence signals were observed in the absence of laser irradiation, suggesting that the production of alkyl radicals by IANM-PEG-FA was mediated by the 808 nm laser and was oxygen-independent. Besides, Vc as an antioxidant could efficiently scavenge the free radicals to inhibit the TDT effects of the IANM-PEG-FA nanosystem. IANM-PEG-FA NPs-mediated intracellular green fluorescence intensity was significantly reduced under 808 nm laser irradiation, paving the way for subsequent evaluation of treatment efficacy. Then, the cytotoxicity of IANM-PEG-FA on 4T1 cells in normoxic and hypoxic environments without laser irradiation was elucidated by a methyl thiazolyl tetrazolium (MTT) assay. As shown in Fig. 4B, the percentage of cell viability remained above 80% after 24 h incubation with IANM-PEG-FA in the 0–100 μg mL^{-1} concentration range, demonstrating that IANM-PEG-FA had low cytotoxicity and did not significantly affect cell growth. However, the overloaded intracellular Zn^{2+} levels could interfere with cell growth and lead to death. The cell viability dropped dramatically to about 18% at concentrations of IANM-PEG-FA up to 200 μg mL^{-1} or even higher. This result would guide the administered dose of IANM-PEG-FA *ex vivo* and *in vivo*. Significantly, IANM-PEG-FA was not toxic to mouse fibroblasts (L929) in the concentration range tested (0–400 μg mL^{-1}) with cell viability above 95% in all cases (Fig. S7†). Next, IANM-PEG-FA (0–100 μg mL^{-1})-mediated antitumor effects *in vitro* of Vc-assisted single PTT and single laser-triggered cascade therapy (PTT and TDT, PTT + TDT) were examined by MTT assay for cell viability. As shown in Fig. 4C, the cell viability decreased in a concentration-dependent manner in both normoxic and hypoxic environments, and synergistic PTT + TDT significantly enhanced the killing efficiency of tumor cells, thus confirming that Vc could effectively inhibit the TDT effects of this nanosystem and demonstrating the superiority of the synergistic treatment. Finally, the live/dead cell co-staining studies were performed to quantitatively and qualitatively visualize the tumor treatment performances of IANM-PEG-FA *in vitro*. As performed in Fig. 4D, normoxic and hypoxic 4T1 cells were irradiated by 1 W cm^{-2} 808 nm laser for 5 min as the Control group had almost no apoptotic cells, and the proportion of living cells in both groups was 99.8%. After co-incubation of 4T1 cells with IANM-PEG-FA for 24 h under dark conditions, the proportions of early apoptotic cells and late apoptotic cells were 15.7% and 4.38% under normoxic conditions, respectively, whereas the total apoptotic rate was slightly elevated to 22.99% under hypoxic condition, which might be attributed to the higher Zn^{2+} release in hypoxic environment resulting in better ion interference treatment effects. For the cells incubated with IANM-PEG-FA and irradiated with 808 nm laser together, the apoptotic cells in normoxia and hypoxia for Vc pretreated single PTT groups reached 36.17% and 35.2% in total, respectively. The cascaded PTT + TDT significantly enhanced the cell lethal effects with early apoptotic cells and late apoptotic cells up to 35.2% and 23.3%, respectively, under normoxia. And the early and late apoptotic cells in hypoxia were 33.7% and 24.0%, respectively. The detailed apoptosis rates and differences of different treatment groups can be seen in the column diagram (Fig. 4E). In addition, the apoptotic regents of calcein-AM (CA)/pyridium iodide (PI) were employed to stain live cells green and dead cells red. As shown in Fig. 4F, the cells without NPs in the dark maintained a healthy growth state under normoxia and hypoxia and almost all the cells were stained with green fluorescence. Moreover, no significant red fluorescence was detected by irradiating the cells with laser only, and there was no significant change in cell viability, indicating that 1 W cm^{-2} 808 nm laser would not kill the cells. IANM-PEG-FA co-incubated with 4T1 cells in dark and under 808 nm laser exposure enabled sustained ion-disrupting therapy (IDT) and cascaded PTT + TDT, respectively. With the support of Vc, IANM-PEG-FA could achieve single PTT effects, allowing for effective assessments of the combined anti-tumor benefits. IDT resulted in distinct red fluorescent dead cells and even large cell detachments under normoxia and hypoxia. The single PTT also showed a large number of dead cells with red fluorescent signals and the trend was close under normoxia and hypoxia. Significantly, synergistic PTT + TDT caused almost total cell death in the irradiated area, and cells in both normoxic and hypoxic environments were stained with red fluorescence. The ratio of semi-quantitative red fluorescence of dead cells to total fluorescence intensity revealed that the cascade of PTT and TDT performed the most significant therapeutic effect (Fig. S8†), which fully demonstrated that IANM-PEG-FA possessed an excellent tumor cell-killing effect. These results suggested that IANM-PEG-FA enabled efficient combined ion-disrupting/photothermal/thermodynamic therapy without oxygen limitation. And single laser-excited multimodal combination therapy not only dramatically enhanced the efficiency of tumor treatment, but also simplified the treatment process, showing great potential for clinical translation.

Biodistribution of IANM-PEG-FA *in vivo*

In light of these encouraging results *in vitro*, IANM-PEG-FA NPs-mediated therapeutic manifestations of synergistic tumor

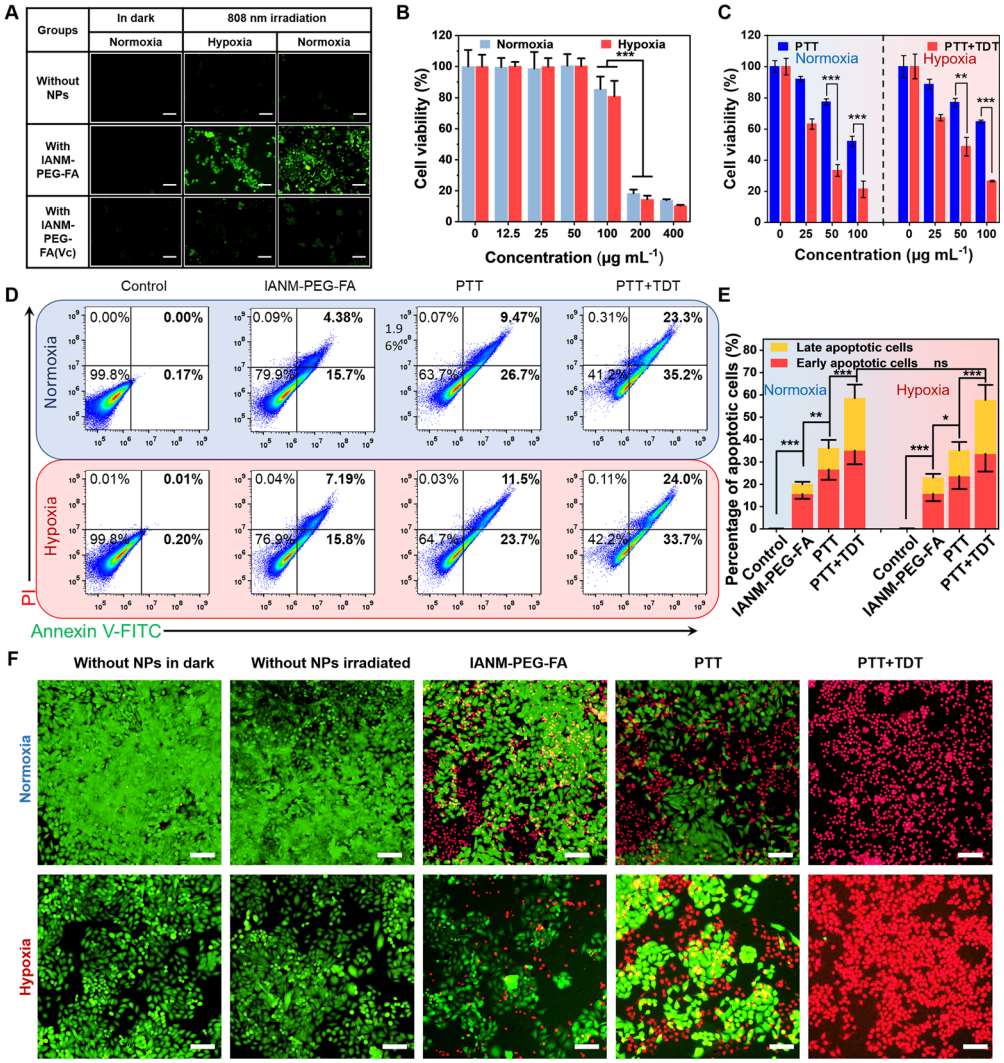

Fig. 4 Antitumor effects *in vitro*. (A) ROS detection in 4T1 cells by DCFH-DA. The scale bar was 100 μm. (B) Relative viabilities of normoxic and hypoxic 4T1 cells incubated with various IANM-PEG-FA concentrations under dark ($n = 6$ biologically independent cellular wells). (C) Cell viabilities of 4T1 cell line treated by single PTT and synergistic PTT/TDT under 808 nm laser irradiation at 1.0 W cm^{-2} for 5 min ($n = 4$ biologically independent cell wells). (D) Quantification of apoptotic 4T1 cells measured by fluorescence-activated cell sorting under normoxic and hypoxic conditions. (E) The detailed percentage of early apoptotic cells and late apoptotic cells. (F) The representative fluorescent images of 4T1 cells co-stained by CA and PI after various experimental treatments under normoxia and hypoxia as indicated on images. The scale bar was 50 μm. Data are presented as mean values ± S.D. ($n = 3$), and P values are calculated by two-tailed Student's t-test. $^{**}P < 0.01$; $^{***}P < 0.001$.

therapy *in vivo* were evaluated. First and foremost, the safety of IANM-PEG-FA *in vivo* was explored by hemolysis analysis and acute toxicity assays. The hemolysis assessment results of IANM-PEG-FA at different concentrations, even up to 500 μg mL^{-1}, were within the safety range of 5% (Fig. S9†). The acute toxicity evaluation is critical for clinical use. Then, the major organs (heart, liver, spleen, lung, kidney) of healthy mice were collected and analyzed by H&E staining after intravenous injection of IANM-PEG-FA with a high dose. As shown in Fig. S10,† no significant abnormality and/or necrosis were found in the tissue sections of the organs in the IANM-PEG-FA and the Saline groups. These results indicated that IANM-PEG-FA did not cause damaging effects in mice and could be safely used for subsequent anti-tumor studies *in vivo*. Next, the circulation time in healthy mice was assessed by the NIR fluorescence imaging features of IANM-PEG-FA. The circulation curve was seen in Fig. 5A, the inset showed NIR fluorescence imaging of blood after IANM-PEG-FA injection at different time points, and the fluorescence intensity gradually decreased. The blood half-life of IANM-PEG-FA was calculated to be 5.24 hours, suggesting good circulatory stability and potential for NIR fluorescence imaging, which contributed to the efficient enrichment of IANM-PEG-FA at the tumor site and precise imaging-guided tumor therapy. Furthermore, 4T1 tumor-bearing mice were utilized to investigate the targeted enrichment and retention effects of IANM-PEG-FA in tumor tissues using a near-infrared fluorescence imager. As shown in Fig. 5B, the tumor-bearing mice were captured at pre-determined time intervals after intravenous injection of IANM or IANM-PEG-FA to visualize the fluorescence distribution. The fluorescence of

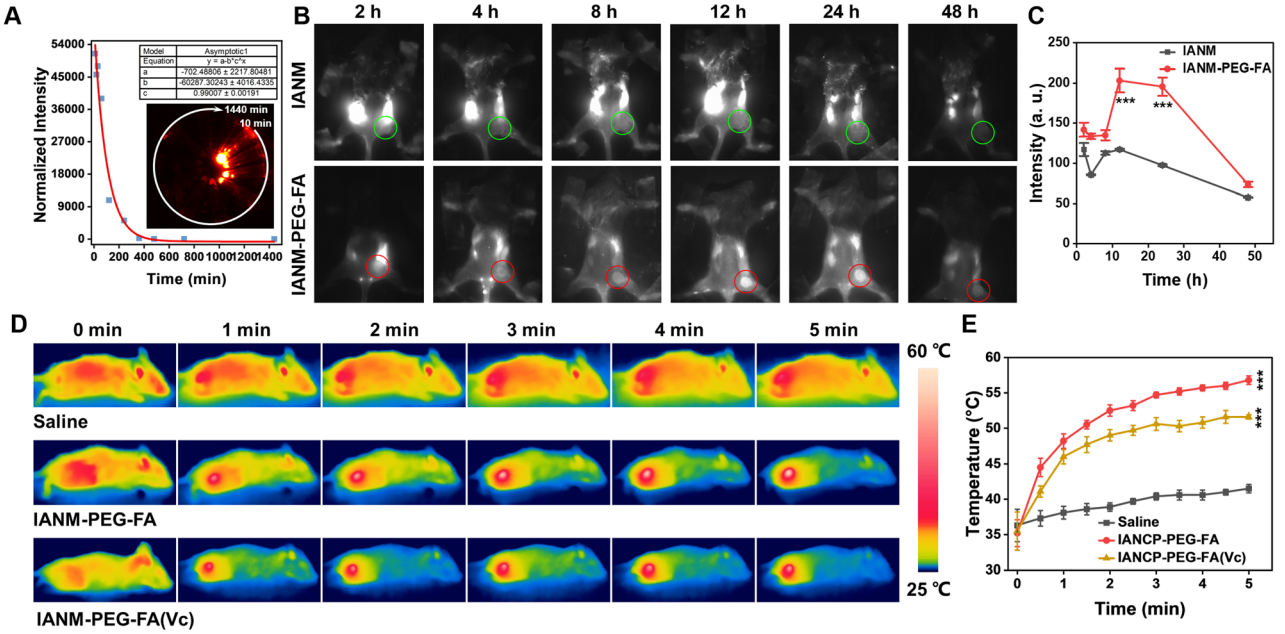

Fig. 5 Biodistribution and photothermal imaging (PTI) capabilities of IANM-PEG-FA in subcutaneous 4T1 xenograft tumor model. (A) Blood circulation curves and fluorescence images as a function of time after intravenous injection of IANM-PEG-FA at different times. (B) Fluorescence changes after the intravenous injection of IANM and IANM-PEG-FA at predetermined interval time, and the tumor areas within the green and red circles, respectively. (C) Fluorescence intensity profiles of tumor regions at corresponding time points. (D) Representative IR thermal images of tumor tissues in 4T1 tumor-bearing mice. (E) Average temperature of tumor tissues as a function of laser irradiation time. Data are presented as mean values ± S.D. ($n = 3$), and P values are calculated by two-tailed Student's t-test ***$P < 0.001$.

the tumor regions in the IANM group marked by the green circle changed insignificantly over time (2–48 h), while the distribution of fluorescence intensity was higher in other parts of the body. Significantly, the fluorescence intensity of tumors labeled with red circles in the IANM group showed precisely tangible changes and reached the maximum at 12 or 24 hours, which indicated that IANM-PEG-FA exhibited good tumor-targeting ability for efficient enrichment and retention. Semi-quantitative analysis of fluorescence at the tumor site showed that the fluorescence intensity in the IANM-PEG-FA group reached its maximum at 12 h and persisted until 24 h (Fig. 5C). The fluorescence intensity of IANM-PEG-FA was significantly different from that of the IANM group due to its targeting ability, suggesting that the modification of PEG–FA facilitated the targeting of IANM to the tumor site. To determine more accurately the enrichment of IANM-PEG-FA in the tumor site and to reflect the tumor-targeting effects of IANM-PEG-FA, the Zn^{2+} content in the tumor tissues was monitored by inductively coupled plasma mass spectrometry (ICP-MS). As displayed in Fig. S11,† the Zn^{2+} content in the IANM-PEG-FA group was 3.33 times higher than that in the IANM group, indicating that IANM-PEG-FA exerted a good tumor-targeting ability and could be more effectively enriched in tumor tissues. Therefore, IANM-PEG-FA was promising to achieve precise and efficient anti-tumor effects with good biocompatibility. Besides, these results could determine the time point of laser irradiation for *in vivo* photothermal therapy to improve treatment efficacy. Subsequently, the photothermal performances of IANM-PEG-FA *in vivo* were evaluated by monitoring the temperature change in the tumor area irradiated by 1 W cm^{-2} 808 nm laser for 5 min. As performed in Fig. 5D, 12 h after intravenous injection of Saline and IANM-PEG-FA solution, the temperature values of tumor-bearing mice were recorded with an infrared thermal imaging camera, especially the tumor tissues irradiated by laser. The body temperature and tumor area temperature of mice in the Saline group did not change significantly from 37 °C to 40 °C with irradiation time, which was lower than the treatment temperature (42 °C), indicating that 1 W cm^{-2} 808 nm laser did not cause damage to the normal tissues of mice. In contrast, the temperature of the tumor area in the IANM-PEG-FA group increased dramatically from the initial 35 °C to 58 °C, which was sufficient to kill tumor cells and ablate tumor tissue. Besides, Vc pre-treated tumor tissues were also significantly heated by 808 nm laser irradiation, and the temperature reached 52 °C from the ordinary temperature of 35.7 °C, suggesting that Vc could mediate IANM-PEG-FA for effective single PTT. The temperature change curves of the tumor tissues irradiated with laser for 5 min were shown in Fig. 5D, which revealed that the photothermal effect induced by 808 nm laser irradiation of IANM-PEG-FA groups was significantly different from that of the Saline group, and the tumor tissues could achieve a good ablation effect. These experiments fully confirmed that IANM could effectively target tumor tissues and provide good NIR fluorescence and photothermal imaging properties to achieve precise tumor treatment.

Antitumor effects *in vivo*

Encouraged by such promising tumor target enrichment and diagnostic outcomes mediated by IANM-PEG-FA *in vitro* and *in*

vivo, 4T1 tumor-bearing mice were further applied to investigate the therapeutic effects of IANM-PEG-FA on mammary tumors. First, when the tumor volume of mice inoculated with 4T1 cells grew to 80–100 mm^3, the tumor-bearing mice were randomly divided into four groups with five mice in each group. Three of these groups of mice were then injected with the low dose of IANM-PEG-FA (5 mg kg^{-1}) *via* the tail vein, while the other group was injected with Saline intravenously as a Control. After the post-injection of 12 h, tumors from Saline and two other groups of IANM-PEG-FA NPs-injected mice were irradiated with a 1 W cm^{-2} 808 nm laser for 5 min, and the Vc-assisted IANM-PEG-FA group was pretreated with intratumoral injection of Vc for 4 h, while the other group of mice injected with IANM-PEG-FA did not undergo any treatment. These groups were named Saline + L, IANM-PEG-FA + L, IANM-PEG-FA + L(Vc) and IANM-PEG-FA, which were used to investigate the safety of Saline irradiated by 808 nm laser and IANM-PEG-FA NPs-mediated multi-modal and single-modal (ion-interfering or photothermal therapy) tumor growth inhibition, respectively, thus demonstrating the superiority of IANM-PEG-FA in 4T1 tumor therapy. After all these treatment procedures, the changes in tumor volume and body weight of each group were recorded every other day for 15 days. As shown in Fig. 6A, the tumor volume time-course curves showed a continuous increase of tumor volume in the Saline + L group without suppression and reached 780 cm^3 at 15 days, indicating that Saline and laser irradiation did not perform a therapeutic effect on tumors. However, the tumor volume growth was slightly inhibited in the IANM-PEG-FA group, which was attributed to tumor cell death due to specific Zn^{2+} interference. Remarkably, the tumor growth inhibition effect of both IANM-PEG-FA + L(Vc) and IANM-PEG-FA + L groups was significantly different from that of the Saline + L group. Moreover, the IANM-PEG-FA + L group was the most effective due to its mediated photothermal/thermodynamic/ionic interference tri-modal treatment effect. Besides, the variability of body weight changes in each group of mice was not significant (Fig. S12†), indicating that IANM-PEG-FA did not affect the growth of mice. The liver and kidney function indicators were also detected to validate the safety of IANM-PEG-FA *in vivo*. As displayed in Fig. S13,† The biomarker concentrations in each group of mice were not significantly different and were within the normal range, indicating that IANM-PEG-FA did not cause metabolic overload and toxic side effects in mice. These results indicated that IANM-PEG-FA exhibited good biocompatibility and could be used to induce efficient tumor therapy at low doses. After 15 days of monitoring, the typical mice and excised tumors were photographed by an optical camera (Fig. 6B). The tumor volume of the Saline + L group grew rapidly and broke through the skin as tumor growth could not be inhibited. The tumor volume was suppressed but not eliminated in all five mice in the IANM-PEG-FA group, thus increasing the risk of metastasis. Significantly, IANM-PEG-FA + L(Vc)-mediated PTT could effectively inhibit tumor growth and completely eliminate 40% of the tumors, which benefited from the high efficiency of PTT and the deep tumor tissue permeability of IANM-PEG-FA. IANM-PEG-FA + L enabled multimodal therapy, resulting in a better tumor treatment efficiency with a cure rate of 80%, which effectively prevented metastasis and recurrence of tumors. The weights of *ex vivo* tumors were also weighed and analyzed (Fig. 6C). Compared to the Saline + L group, the other three groups showed differences, and the IANM-PEG-FA + L(Vc) and IANM-PEG-FA + L groups were significantly different. In addition, there was a significant difference between the IANM-PEG-FA group and the IANM-PEG-FA + L group, indicating that multimodal treatment significantly inhibited tumor growth and effectively eliminated tumors. Next, the therapeutic effects were studied by the histopathological analysis of tumor tissues. As depicted in Fig. 6D, Hematoxylin and eosin (H&E) staining showed intact tumor tissue without significant abnormalities and lesions in the Saline + L group, whereas the other three groups all showed extensive tissue necrosis (the area circled by green lines). It was clear from the size of the area that the IANM-PEG-FA + L group had the largest necrotic area of tumor tissue. Meanwhile, the immunofluorescent staining of TUNEL revealed results consistent with those of H&E staining (Fig. 6E). The apoptotic and necrotic cells in the IANM-PEG-FA + L group were stained with the greatest intensity and area of green fluorescence. These results fully confirmed that low doses of IANM-PEG-FA could still achieve excellent anti-tumor effects with good biosafety, providing a new strategy for clinical cancer treatment.

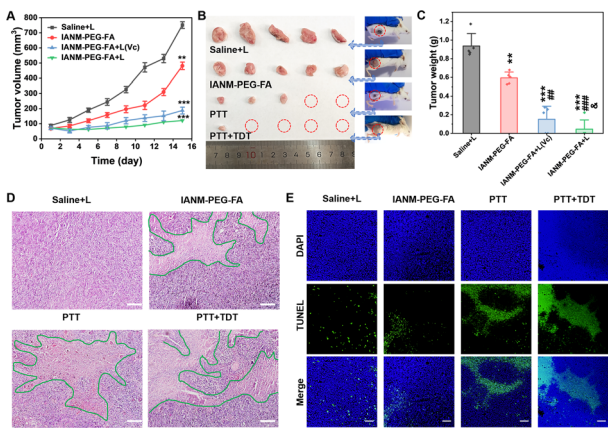

Fig. 6 Anti-tumor effects of IANM-PEG-FA *in vivo*. (A) Tumor growth curves of mice receiving various treatments. (B) Optical pictures of tumor-bearing mice and *ex vivo* tumors after treatment. (C) Tumor weight of *ex vivo* tumors after completion of treatment. (D) Representative H&E images of tumor tissue sections of mice in different groups. The scale bars were 100 μm. (E) TUNEL images of tumor tissues of treated mice. The scale bars were 100 μm. Data are presented as mean values ± S.D. ($n = 5$), and P values are calculated by two-tailed Student's t-test. $^{**}P < 0.01$ and $^{***}P < 0.001$ compared to the Saline + L group, & $P < 0.05$ compared to the IANM-PEG-FA + L(Vc) group, $^{\#\#}P < 0.01$ and $^{\#\#\#}P < 0.001$ compared to the IANM-PEG-FA group.

Conclusions

In summary, we facilely developed a carrier-free nanosystem, IANM-PEG-FA, with oxygen-irrelevant cascade PTT and TDT capabilities and pH-responsive ion-disturbing therapeutic

effects for efficient hypoxic tumor synergistic therapy at low doses. IANM-PEG-FA was prepared by efficiently encapsulating ICG through the coordination process of Zn^{2+} with the alkyl radical initiator of AIPH, and further modifying PEG–FA. PEG–FA moieties enabled the nanosystem with prolonged circulatory stability and active tumor targeting features, greatly enhancing tumor enrichment and retention efficiency. The coordination polymer NPs would degrade and release Zn^{2+}, AIPH and ICG in the mildly acidic environment of tumors, enabling lysosomal escape and deep penetration. High concentrations of Zn^{2+} could interfere with the growth of tumor cells, performing ion-disturbing therapeutic effects. ICG not only acted as the PTA and NIR fluorescence imaging contrast agent but also triggered the production of alkyl radicals by AIPH, resulting in the precise photothermal and thermodynamic cascade of single-laser-induced therapeutic effects. Besides, this nanosystem could effectively improve the photothermal stability of ICG, and its photothermal effect can further promote the release efficiency, which was crucial for improving the therapeutic efficacy of this nanosystem. IANM-PEG-FA NPs-mediated trimodal therapies are not limited to oxygen and promote each other, showing promising applications in the clinical treatment of hypoxic tumors. *In vitro* and *in vivo* studies fully confirmed that IANM-PEG-FA exhibited good biocompatibility and precise anti-tumor effect guided by fluorescence imaging with targeted effect. Tumor elimination rate of 80% to effectively prevent metastasis and recurrence, which shed new light on the design of simple materials with high antitumor outcomes.

Data availability

All data included in this study are available upon request from the corresponding author. The data supporting this article have been included as part of the ESI.†

Author contributions

L. H. conceived the project idea, analyzed the data, and wrote the paper. L. H. prepared and characterized the nanosystem. L. H., G. D. and S. L. performed the cell and animal experiments. All authors read and edited the manuscript. CRediT: Liefeng Hu writing – original draft, conceptualization, methodology, visualization, formal analysis, funding acquisition; Ganlin Dong investigation, formal analysis; Xiaohong Li investigation, formal analysis, data curation; Shuting Li investigation, methodology, writing – review & editing; Yonggang Lv data curation, formal analysis, writing – review & editing, funding acquisition, supervision.

Conflicts of interest

The authors declare no competing financial interest.

Acknowledgements

This work was supported by National Natural Science Foundation of China (U23A2070), Natural Science Foundation of Hubei Province, China (2022CFA023) and State Key Laboratory of New Textile Materials and Advanced Processing Technologies (FZ20230024). We also thank Dr Wang and Xiong from the Analytical and Testing Center of Wuhan Textile University for the technical assistance on CLSM and TEM.

References

1 X. Li, J. F. Lovell, J. Yoon and X. Chen, *Nat. Rev. Clin. Oncol.*, 2020, **17**, 657–674.
2 J. Yang, M. Hou, W. Sun, Q. Wu, J. Xu, L. Xiong, Y. Chai, Y. Liu, M. Yu, H. Wang, Z. P. Xu, X. Liang and C. Zhang, *Adv. Sci.*, 2020, **7**, 2001088.
3 M. Overchuk, R. A. Weersink, B. C. Wilson and G. Zheng, *ACS Nano*, 2023, **17**, 7979–8003.
4 J. Sun, X. Cai, C. Wang, K. Du, W. Chen, F. Feng and S. Wang, *J. Am. Chem. Soc.*, 2021, **143**, 868–878.
5 J. Huo, Q. Jia, H. Huang, J. Zhang, P. Li, X. Dong and W. Huang, *Chem. Soc. Rev.*, 2021, **50**, 8762–8789.
6 S. Zhao, S. Wu, Q. Jia, L. Huang, M. Lan, P. Wang and W. Zhang, *Chem. Eng. J.*, 2020, **388**, 124212.
7 L. Hu, J. Cao and Y. Lv, *Chem. Eng. J.*, 2024, **492**, 152270.
8 L. Hu, C. Xiong, J. J. Zou, J. Chen, H. Lin, S. J. Dalgarno, H. C. Zhou and J. Tian, *ACS Appl. Mater. Interfaces*, 2023, **15**, 25369–25381.
9 H. Wang, K. F. Xue, Y. Yang, H. Hu, J. F. Xu and X. Zhang, *J. Am. Chem. Soc.*, 2022, **144**, 2360–2367.
10 B. Tian, C. Wang, Y. Du, S. Dong, L. Feng, B. Liu, S. Liu, H. Ding, S. Gai, F. He and P. Yang, *Small*, 2022, **18**, 2200786.
11 Z. Wen, F. Liu, G. Liu, Q. Sun, Y. Zhang, M. Muhammad, Y. Xu, H. Li and S. Sun, *J. Colloid Interface Sci.*, 2021, **590**, 290–300.
12 L. Hu, Y. Xu, Y. Zhao, Z. Mei, C. Xiong, J. Xiao, J. Zhang and J. Tian, *Chem. Eng. J.*, 2023, **476**, 146829.
13 R. Y. Meng, Y. Zhao, H. Y. Xia, S. B. Wang, A. Z. Chen and R. K. Kankala, *ACS Mater. Lett.*, 2024, **6**, 1160–1177.
14 Y. Li, D. Hu, M. Pan, Y. Qu, B. Chu, J. Liao, X. Zhou, Q. Liu, S. Chen, Y. Chen, Q. Wei and Z. Qian, *Biomaterials*, 2022, **288**, 121700.
15 D. Li, X. Chen, D. Wang, H. Wu, H. Wen, L. Wang, Q. Jin, D. Wang, J. Ji and B. Z. Tang, *Biomaterials*, 2022, **283**, 121476.
16 M. Overchuk, R. A. Weersink, B. C. Wilson and G. Zheng, *ACS Nano*, 2023, **17**, 7979–8003.
17 L. Song, B. Chen, Z. Qin, X. Liu, Z. Guo, H. Lou, H. Liu, W. Sun, C. Guo and C. Li, *Adv. Healthcare Mater.*, 2022, **11**, 2102298.
18 H. Dou, Z. Luo, H. Wang, Q. Duan, Z. Jiang, H. Chen and N. Tan, *Chem. Eng. J.*, 2024, **487**, 150523.
19 D. Gao, T. Chen, S. Chen, X. Ren, Y. Han, Y. Li, Y. Wang, X. Guo, H. Wang, X. Chen, M. Guo, Y. S. Zhang, G. Hong, X. Zhang, Z. Tian and Z. Yang, *Nano–Micro Lett.*, 2021, **13**, 1–21.
20 X. Liu, Y. Yang, M. Ling, R. Sun, M. Zhu, J. Chen, M. Yu, Z. Peng, Z. Yu and X. Liu, *Adv. Funct. Mater.*, 2021, **31**, 2101709.
21 Y. Dai, H. Zhao, K. He, W. Du, Y. Kong, Z. Wang, M. Li, Q. Shen, P. Sun and Q. Fan, *Small*, 2021, **17**, 2102527.

22 X. Li, Y. W. Jiang, W. J. Tang, S. Yue, W. Wang, H. Yao, J. Xu, Z. Chen and J. J. Zhu, *Small Methods*, 2024, 2400697.
23 H. Sun, Q. Zhang, J. Li, S. Peng, X. Wang and R. Cai, *Nano Today*, 2021, **37**, 101073.
24 J. Yang, R. Xie, L. Feng, B. Liu, R. Lv, C. Li, S. Gai, F. He, P. Yang and J. Lin, *ACS Nano*, 2019, **13**, 13144–13160.
25 Y. Wan, G. Lu, J. Zhang, Z. Wang, X. Li, R. Chen, X. Cui, Z. Huang, Y. Xiao, J. Chelora, W. Zhang, Y. Liu, M. Li, H. Y. Xie and C. S. Lee, *Adv. Funct. Mater.*, 2019, **29**, 1903436.
26 W. Li, B. Li, B. Wu, B. Tian, X. Chen, C. Wang, W. Hong and J. Peng, *ACS Appl. Mater. Interfaces*, 2022, **14**, 29563–29576.
27 W. Zhang, H. Zhou, D. Gong, H. Wu, X. Huang, Z. Miao, H. Peng and Z. Zha, *Adv. Healthcare Mater.*, 2023, **12**, 2202947.
28 W. Wang, X. Zhang, X. Ni, W. Zhou, C. Xie, W. Huang and Q. Fan, *Biomater. Sci.*, 2022, **10**, 846–853.
29 Q. Li, Y. Zhang, X. Huang, D. Yang, L. Weng, C. Ou, X. Song and X. Dong, *Chem. Eng. J.*, 2021, **407**, 127200.
30 L. H. Liu and X. Z. Zhang, *Prog. Mater. Sci.*, 2022, **125**, 100919.
31 S. Karaosmanoglu, M. Zhou, B. Shi, X. Zhang, G. R. Williams and X. Chen, *J. Controlled Release*, 2021, **329**, 805–832.
32 H. Mei, S. Cai, D. Huang, H. Gao, J. Cao and B. He, *Bioact. Mater.*, 2022, **8**, 220–240.
33 W. J. Choi, S. H. Lee, B. C. Park and N. A. Kotov, *J. Am. Chem. Soc.*, 2022, **144**, 22789–22804.
34 G. Huang, Y. Qiu, F. Yang, J. Xie, X. Chen, L. Wang and H. Yang, *Nano Lett.*, 2021, **21**, 2926–2931.
35 L. Li, H. Tian, Z. Zhang, N. Ding, K. He, S. Lu, R. Liu, P. Wu, Y. Wang, B. He, M. Luo, P. Peng, M. Yang, E. C. Nice, C. Huang, N. Xie, D. Wang and W. Gao, *ACS Appl. Mater. Interfaces*, 2022, **15**, 452–468.
36 H. Wang, F. Lin, Y. Wu, W. Guo, X. Chen, C. Xiao and M. Chen, *ACS Nano*, 2023, **17**, 12176–12187.
37 M. K. Shim, S. Yang, I. C. Sun and K. Kim, *Adv. Drug Delivery Rev.*, 2022, **183**, 114177.
38 J. W. Wang, Q. W. Chen, G. F. Luo, P. Ji, Z. Y. Han, W. F. Song, W. H. Chen and X. Z. Zhang, *Nano Lett.*, 2022, **22**, 8735–8743.
39 J. Zhou, K. Li, H. Qin, B. Xie, H. Liao, X. Su, C. Li, X. He, W. Chen and X. Jiang, *J. Colloid Interface Sci.*, 2023, **637**, 453–464.
40 D. Gao, Y. Shi, J. Ni, S. Chen, Y. Wang, B. Zhao, M. Song, X. Guo, X. Ren, X. Zhang, Z. Tian and Z. Yang, *Small*, 2022, **18**, 2106000.
41 Z. Fu, Y. Lin, H. Xiao, H. Wang, Y. Liu, Y. Gong, L. Li, X. Chen, C. Li, C. Ding and C. Lu, *ACS Mater. Lett.*, 2024, **6**, 2582–2590.
42 C. Lv, W. Kang, S. Liu, P. Yang, Y. Nishina, S. Ge, A. Bianco and B. Ma, *ACS Nano*, 2022, **16**, 11428–11443.